Aalto University

OPEN ACCESS

This is an electronic reprint of the original article.
This reprint may differ from the original in pagination and typographic detail.

Mäkinen, Tero; Parmar, Anshul D.S.; Bonfanti, Silvia; Alava, Mikko J.

Avalanches in Cu-Zr-Al metallic glasses

Published in:
Physical Review E

DOI:
10.1103/PhysRevE.111.014107

Published: 03/01/2025

Document Version
Publisher's PDF, also known as Version of record

Please cite the original version:
Mäkinen, T., Parmar, A. D. S., Bonfanti, S., & Alava, M. J. (2025). Avalanches in Cu-Zr-Al metallic glasses. *Physical Review E*, *111*(1), 1-9. Article 014107. https://doi.org/10.1103/PhysRevE.111.014107

This material is protected by copyright and other intellectual property rights, and duplication or sale of all or part of any of the repository collections is not permitted, except that material may be duplicated by you for your research use or educational purposes in electronic or print form. You must obtain permission for any other use. Electronic or print copies may not be offered, whether for sale or otherwise to anyone who is not an authorised user.

Avalanches in Cu-Zr-Al metallic glasses

Tero Mäkinen,[1,*,†] Anshul D. S. Parmar,[2,*,‡] Silvia Bonfanti,[2] and Mikko J. Alava[1,2]
[1]*Department of Applied Physics, Aalto University, P. O. Box 15600, 00076 Aalto, Espoo, Finland*
[2]*NOMATEN Centre of Excellence, National Center for Nuclear Research, ul. A. Soltana 7, 05-400 Swierk/Otwock, Poland*

(Received 24 September 2024; accepted 10 December 2024; published 3 January 2025)

Metallic glasses have mechanical properties, which exhibit avalanches in the disguise of stress drops. We study these phenomena in a classical metallic glass system Cu-Zr-Al by athermal quasistatic shear and varying the element concentrations and for pure Cu-Zr 50/50 case the cooling rate. The resulting mechanical properties are close to the behavior found experimentally. At small strains, the pristine systems are akin to other glassy systems with a so-called gap distribution with a small positive exponent. Critical avalanching behavior is found only approaching the yield point. The post-yield stress drops are universal, and the gap distribution becomes flat.

DOI: 10.1103/PhysRevE.111.014107

I. INTRODUCTION

Despite the no-long-range structural order, metallic glasses (MGs) exhibit elasticity to the external shear and will flow if sufficient shear stress is applied. The plasticity can be conceived as consisting of elementary rearrangements, which are localized in the so-called shear transformation zones (STZs), but display long-range elastic interactions. Below a critical strain, the events are localized [1–4] and result in crackling noise, like stress drops. The piecewise elastic response is intersected with these plastic stress drops and as one approaches the yield point, the plastic events manifest as nonlocalized avalanches, and finally, the system reaches a well-defined steady state.

As an elementary observation, the statistics of such plastic excitations correlate with the microscopic description. The probability distribution function $p(\Delta\gamma;\gamma)$ in the strain interval over accumulated strain γ is defined by the additional shear strain $\Delta\gamma$ required to trigger an avalanche at the strain γ [5–7]. This is conceptually useful also in order to make a connection to depinning transition theory [8]. The empirical pseudogap, i.e., $\lim_{\Delta\gamma\to 0} p(\Delta\gamma;\gamma=0^+) \propto \Delta\gamma^\theta$ is characterized by the power-law behavior of the $\Delta\gamma$ distribution at small values. The exponent θ does not claim any universality and is found to be dimension and glass preparation protocol dependent [6,8,9]. However, as the yield is approached from below, initially, the exponent rapidly drops and in the steady state becomes zero beyond the yield strain [7,9,10]. In the simplistic picture, in response to the deformation, the plastic rearrangements and their spatial and temporal correlations can be considered in the context of the pinning to depinning transition [11], making a depinning event the epicentre of an avalanche. The role of the critical threshold in the depinning against the flow and the growth of the local strain can explicitly be considered for the macroscopic yield stress and the shear band [11–13].

The studies of model glass systems by molecular dynamics extend over a long period of time with the main questions being asked concentrating on the critical exponents of the yield transition and the effects of inertia and temperature [6,14]. These naturally have been based on the STZ and depinning analogies, and later this work has expanded to consider the effect of sample preparation or cooling. The current understanding points toward a critical point in disorder, separating systems with a finite stress drop ("good glasses") from those with no drop ("bad glasses") [15]. While this is indicated by mean-field arguments, the properties of the steady-state beyond the yield stress and the approach to that are an open question in terms of universality, apart from the generic idea of a gap distribution, applied both below and above the yield stress.

Recently some work has been done on more realistic (metallic) glass models, including the Cu-Zr system, including aspects like the geometric details of the yield events as plastic strain develops [16–19] with partial evidence for the avalanche statistics in general. One may confront these with generic glass criticality [15], and generally a stress drop exponent for the distribution $p(\Delta\tau)$ of stress drops $\Delta\tau$ emerges with a value of about 1.2, . . . , 1.4. As usual, the distribution is via its cutoff $\Delta\tau_0$ coupled to the value of the mean drop at a given strain, $\langle\Delta\tau\rangle$ as noted by Shang *et al.* [20]. Interestingly, in the Lennard-Jones system studied, power-law-like activity was found for small γ.

The Cu-Zr-(Al) system is the ubiquitous metallic glass for its good glass forming ability and the possibility of controlling its properties again by cooling but also by composition. In particular, it was recognized some time ago [21] that aluminum brings beneficial effects as it seems by forming local structural motifs to improve mechanical properties. Thus, it is of interest to compare this key glass family *in silico* to expectations from glass theory and to experimental observations.

For instance, the experimental work of Das *et al.* [22] shows that the composition $Cu_{47.5}Zr_{47.5}Al_5$ has superior

*These authors contributed equally to this work.
†Contact author: tero.j.makinen@aalto.fi
‡Contact author: Anshul.Parmar@ncbj.gov.pl

 ©2025 American Physical Society

mechanical properties, such as higher strength, improved ductility, and work hardenability, compared to the binary $Cu_{50}Zr_{50}$, prepared by arc melting. The same optimal 5% Al was found by Yu and Bai [23] when considering maximal plastic strain and also the Poisson ratio. Furthermore, it has been shown by Pauly *et al.* [24] that the addition of Al increases tensile failure stress and elastic modulus, but decreases the plastic strain. In nanoindentation experiments, Poltronieri *et al.* [25] found an increase in shear and elastic moduli as well as hardness with increasing Al content (up to 12%). Similarly, Cheung and Shek [26] in their nanoindentation experiments found an increase in hardness and elastic modulus with increasing Al content (up to 10%). Additionally, they saw a decrease in creep displacement.

Regarding the avalanches, there has only been a few experimental studies of the Cu-Zr-Al system [27–29]. These have either found very nonuniversal avalanche size exponents [28] (ranging from 1.01 to 1.70) or mean-field behavior [29]. Also other experimental studies of MG systems, such as Zr-Hf-Nb-Cu-Ni-Al [30–33] and Zr-Cu-Ni-Al [34,35], have reported mean-field behavior. All of these experimental studies have been conducted with relatively limited datasets.

The structure of this paper is as follows. In the next section, we briefly go through the methodology needed to study the shear response of MGs *in silico*. The results part is divided roughly into three themes: the generic mechanical properties and their dependence on cooling (pure Cu-Zr) and composition, the small-strain regime before yielding, and the statistics of yielding in the steady state after that. Finally, we finish with a summary.

II. METHODS

Simulation methods. Metallic glass samples are simulated using molecular dynamics methods implemented in LAMMPS [36], where the interactions are modeled through the embedded atom method (EAM) as developed by Ref. [37]. The simulations are performed in a cubic box with periodic boundary conditions in three dimensions. We vary the element concentrations, system sizes N, and cooling rates $\dot{T}$ as reported in Table I. The compositions are illustrated in a ternary plot in Fig. 1.

Hybrid molecular dynamics algorithm. To generate metallic glasses we employ a hybrid molecular dynamics + Monte Carlo (MD + MC) scheme under the variance-constrained semigrand canonical ensemble (VC-SGC) [38]. This VC-SGC MC scheme allows exploring the configurational degrees of freedom by randomly selecting an atom and attempting to change its type, while also calculating the corresponding energy and concentration changes. It allows to target specific concentration ranges while maintaining a fixed total number of particles and volume. Acceptance of these transmutations follows the Metropolis criterion, ensuring the preservation of detailed balance. On the other hand, the relaxation processes are accounted for by the MD integration steps. To maintain the desired concentration within the system [38], we set the variance parameter $\kappa = 10^3$. The differences in chemical potential relative to Zr using hybrid MD + MC simulations under the semigrand canonical ensemble at a temperature of 2000 K and the specific set of parameters that minimize the composition errors in relation to the desired concentration can be found in Ref. [39]. The hybrid scheme is also used for Cu-Zr by Ref. [40].

TABLE I. Averaged mechanical parameters for the compositions used (systems of size 6000 shown in Fig. 2). The columns are system size N, the cooling rate $\dot{T}$, the shear modulus G, the maximum shear stress τ_{max}, and the strain corresponding to the maximum stress γ_{max}.

Composition	N	$\dot{T}$ [K/s]	G [GPa]	τ_{max} [GPa]	γ_{max}
$Cu_{0.50}Zr_{0.50}$	6000	10^{11}	24.74	1.811	0.1095
$Cu_{0.50}Zr_{0.50}$	6000	10^{12}	23.74	1.760	0.1035
$Cu_{0.50}Zr_{0.50}$	6000	10^{13}	22.90	1.537	0.1035
$Cu_{0.50}Zr_{0.50}$	6000	10^{14}	20.47	1.049	0.0945
$Cu_{0.50}Zr_{0.50}$	6000	10^{15}	16.95	0.845	0.9025
$Cu_{0.30}Zr_{0.70}$	6000	10^{12}	19.00	0.987	0.0945
$Cu_{0.70}Zr_{0.30}$	6000	10^{12}	24.84	1.580	0.1065
$Cu_{0.47}Zr_{0.47}Al_{0.06}$	6000	10^{12}	24.00	1.743	0.1005
$Cu_{0.45}Zr_{0.45}Al_{0.10}$	6000	10^{12}	24.93	1.736	0.1045
$Cu_{0.40}Zr_{0.40}Al_{0.20}$	6000	10^{12}	26.59	1.799	0.1095
$Cu_{0.37}Zr_{0.37}Al_{0.26}$	6000	10^{12}	28.35	1.845	0.1115
$Cu_{0.50}Zr_{0.50}$	3000	10^{12}	23.43	1.667	0.1025
$Cu_{0.50}Zr_{0.50}$	12000	10^{12}	23.17	1.798	0.1025
$Cu_{0.50}Zr_{0.50}$	24000	10^{12}	23.96	1.834	0.1045

Quenching protocol. The glass state is obtained through quenching in the isobaric-isothermal ensemble (NpT) from the liquid at 2000 K to 300 K using a cooling rate reported in Table I and a time step $\Delta t = 1$ fs. For the MD + MC scheme, every 20 MD steps, a MC cycle consisting of $N/4$ attempts is performed. The cooling process is performed by integrating the Nosé-Hoover equations with damping parameters $\tau_T = 2$ fs and $\tau_p = 5$ ps for the thermostat and barostat. All results are obtained keeping the external pressure $P = 0$.

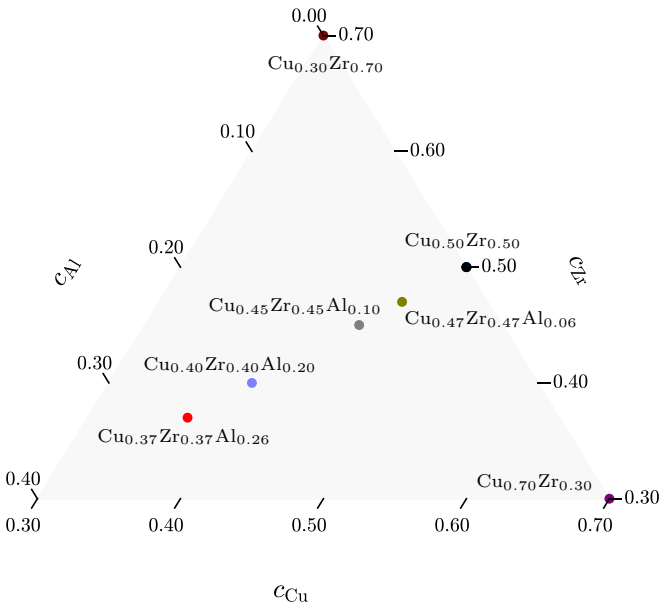

FIG. 1. Ternary plot of the compositions used (other parameters listed in Table I).

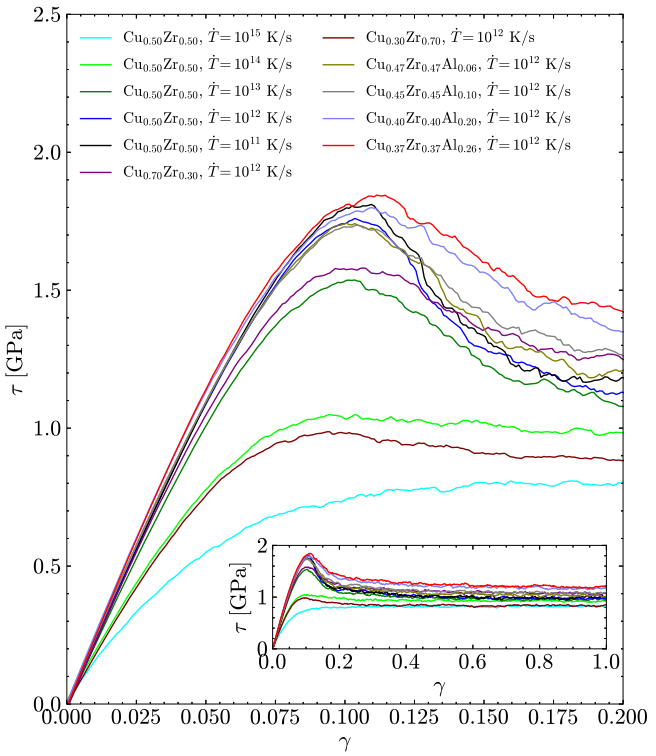

FIG. 2. The averaged stress-strain curves for various compositions and cooling rates $\dot{T}$ (for $N = 6000$). The inset shows a zoomed-out view of the same data up to $\gamma = 1$, showing the steady-state behavior.

Athermal quasistatic shear. The shear simulations are performed for the samples cooled to $T = 300$ K. The simulation box is incrementally sheared along the x direction with respect to the y direction by $\delta\gamma = 10^{-4}$, and at each strain increment, MD simulations are performed for a duration of 1 ps. Throughout the shearing process, we record the stress-strain response, which provides a detailed stress-strain curve for analysis (see Fig. 2). From the stress-strain curves, we determine the shear modulus G, by averaging the positive slopes of the stress-strain curve for the first 1% of strain in each configuration. The maximum stress $\tau_{\max}$ and the corresponding strain γ_y (shown in Table I) are then determined from the stress-strain curve averaged over all the configurations, by taking the point corresponding to the maximum stress.

The stress drops are determined by looking at the periods when the stress τ is decreasing. The drop size $\Delta\tau$ is the difference between the the point where the stress started to decrease and the point when it starts to increase again. Drops smaller than 10^{-4} GPa are discarded as noise. This threshold is arbitrary but corresponds to a point where the stress drop distribution starts to become flat. The strain increments $\Delta\gamma$ are then the lengths of the periods between the end of a previous stress drop and the start of the subsequent drop.

Maximum likelihood fitting. The distributions observed are fitted using the maximum likelihood method [41]. For a dataset x_i (i ranging from 1 to N_x) and a probability density function $p(x;\phi_j)$, where ϕ_j are the parameters for the distribution, one computes the parameters that maximize the likelihood function $\mathcal{L}(\phi_j) = \prod_{i=1}^{N_x} p(x_i;\phi_j)$, which are the optimal parameters.

For the case of the Weibull distribution we emphasize the pseudogap part of the distribution, and initially do the fitting only from zero to a value $\Delta\gamma = 10^{-3}$ corresponding roughly to the mode of the distribution. Fixing this estimate for the pseudogap exponent θ, we then fit the full distribution, using the whole dataset.

III. RESULTS

A. Generic behavior

Figure 2 and Table I show the main features of different compositions and/or cooling rates as regards the typical mechanical properties under shear. The curves of Fig. 2 (averages of 100 runs each) split roughly into two groups: ones with a pronounced stress peak (which makes it easy to define yield stress) and ones without. The latter consists of a 30/70 Cu-Zr mixture and two very fast-cooled 50/50 cases. The highest yield stresses are achieved with high Al contents, but the sharpest peaks with the slowest cooling rates. The decrease in peak sharpness—increased ductility—agrees with the experimental observations [22,23]. Table I shows the resulting mechanical characteristics with clear trends for the elastic modulus and peak/yield stress with the cooling rate and, likewise, a weaker but still clear trend with the addition of Al to the equiatomic Cu-Zr composition. The results of Table I for different N give some confidence limits to the values quoted, as there is a slight trend with N. The effect of Al is in agreement with the experimental picture (e.g., Ref. [25]) in that the shear modulus shows a clear but nondrastic increase with Al. Note that the change in the yield stress is in relative terms larger. After the peak, the systems enter a flow state with the flow stress following the same order from case to case (see inset of Fig. 2).

B. Development of plastic deformation

Next, we consider the effects of cooling and composition with the microscopic picture of the plastic deformation. In the presence of an avalanche, the system can be viewed as the plastically deformed particles as the core and the rest of the system undergoing an elastic deformation in response to the stresses created by the imposed strain. To this end, we first estimate the particles participating in a plastic deformation by considering the nonaffine displacement of particles. It is observed that the distribution of single-particle displacements $p(dr)$ displays a power-law elastic profile with an exponential tail at the cutoff. The deviations from the power law account for the particles "participating" in the plastic deformations [42]. Figure 3 shows the distribution of single-particle displacements for the plastic events in various windows of strain. The exponent of the power law, however, is found to be sensitive to the window of the strain and system preparation history [43]. The choice of the cutoff appears to be independent of the system preparation protocols, strain, and the additional concentration of Aluminum. Particles are considered "plastic" if they are displaced by more than 0.3 Å. With this cutoff in the particle displacements, we wish to include particles

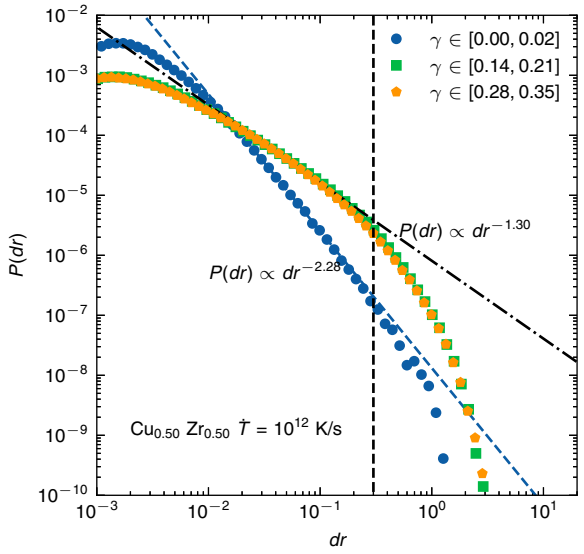

FIG. 3. Distributions of the particle's nonaffine displacements at the plastic events shown in log-log scale for various strain intervals for a system of $Cu_{50}Zr_{50}$ with the cooling rate $\dot{T} = 10^{12}$ K/s for 6000 particles. The particles are considered plastic/active if the nonaffine displacement corresponds to the tails of the distribution, marked as $dr \geqslant 0.3$ Å [42].

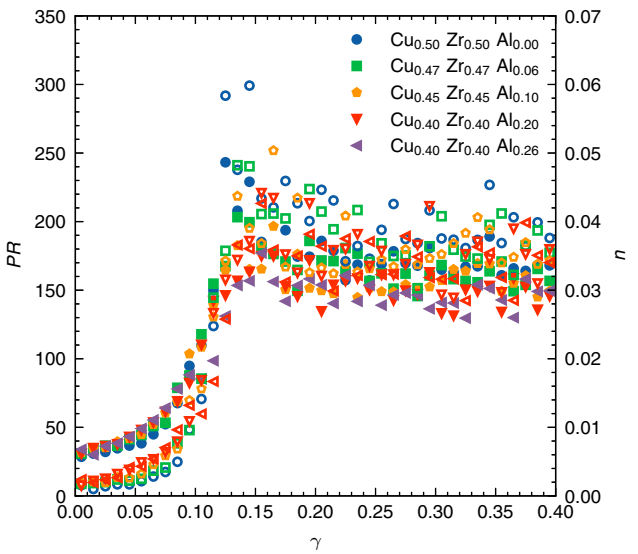

FIG. 4. The participation ratio (PR, filled symbols) and the fraction of particles in plasticity (n, open symbols) for the various concentrations of Al remains the same across the yield.

that take part in the plastic deformation, and exclude particles undergoing elastic response.

The microscopic nature of the plastic deformation is defined by two different approaches. First, we observe the fraction of the particles involved in the plastic response at the avalanche, i.e., $n = N_{pl}/N$, where N_{pl} is the number of particles displaced by more than the cutoff 0.3 Å. For the second approach, we study the extent of localization of particle rearrangements resulting from the transitions between basins at the avalanches. We measure the number of involved particles in the basin's transition to the plastic event by the participation ratio (PR), defined as

$$\mathrm{PR} = \frac{\left[\sum_{i=1,N} dr_i^2\right]^2}{\sum_{i=1,N} dr_i^4}, \tag{1}$$

where dr_i is the displacement of particle 'i' between basins at the plastic event. In the plastic event, the PR would yield the total mobile particles involved in the transition.

Figure 4 shows the fraction of plastic particles and the parameter-free description of the avalanche by the participation ratio for the various concentrations of Al and the strain across the tentative yield point. The introduction of the various concentrations of Al has little effect to contribute to the deformation and does not affect the nature of the avalanches at the microscopic level.

Once established that the nature of avalanches is independent of the compositions, we further focus on the cooling rates dependent on the avalanches for the Cu-Zr system. To discover the role of cooling in the local stability of the particles against the mechanical deformations, we record the strain for each particle for the first plastic event. Figure 5 shows the distribution of the particle undergoing the first plastic event for the various cooling rates for the Cu-Zr glass. The fraction of particles undergoing the first avalanche for the $\gamma \to 0$ can be found consistent with the marginal stability in the glasses [7]. In better-annealed glasses with high stability, a larger fraction of particles undergo the first plastic event in the narrow strain window near the yield. This is consistent with the increasing brittlelike response as the yield approaches. Meanwhile, the yield is gradual for poor glasses, and particles undergo the first plastic deformation across a wide range of strain values.

The question that naturally arises is "how are the plastic events spatially distributed?" Figure 6 shows the spatial arrangement of the particles undergoing the first plastic event

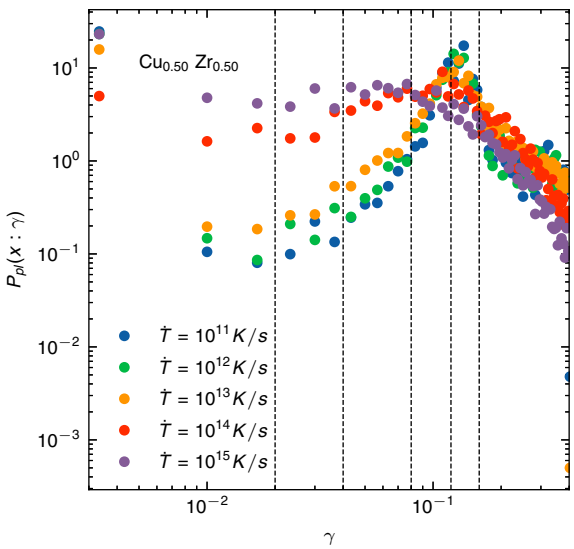

FIG. 5. The distribution of the particle undergoing the first yield event. In better annealed glasses more particles participate around the yield, which is coherent with the conventional ductile-to-brittle response. The dashed lines indicate the strains used in the snapshots in Fig. 6.

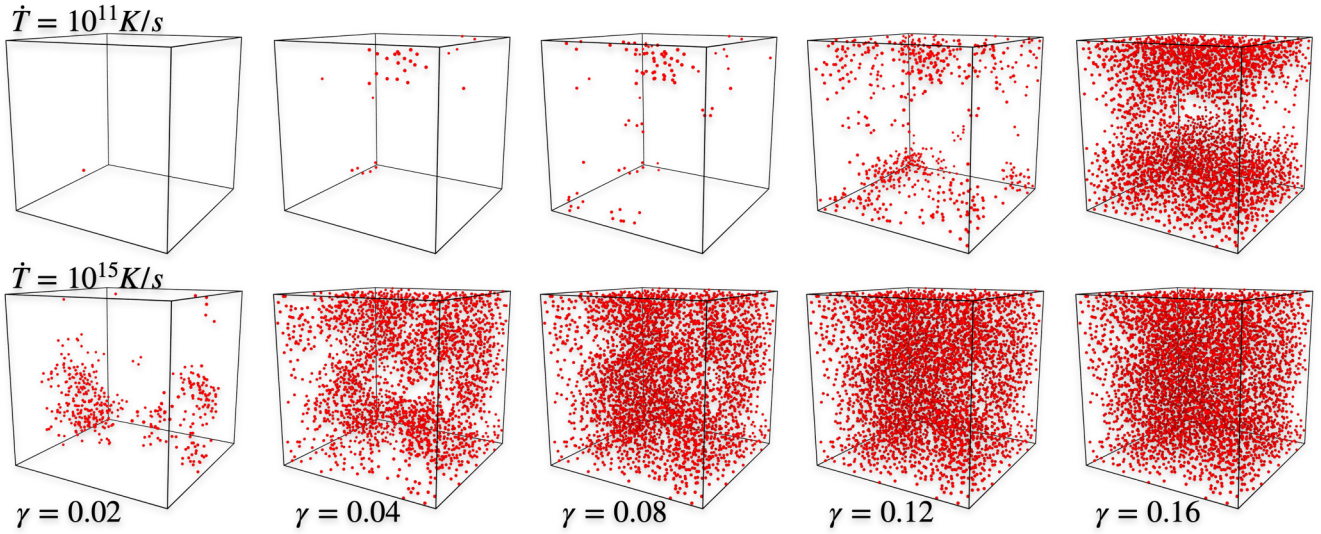

FIG. 6. The spatial profile of the particles undergone the first plastic event. Compared with the poor glass, the well-relaxed glass shows localized plastic events, which act as the nucleation points for the additional plastic events.

for a range of strain and cooling rates, incising better and poorly annealed glasses. For the poor glass, the first plasticity for particles is observed to be strain independent, highlighting the presence of numerous soft zones and underlying complex elastic interactions. Whereas, for the well-annealed glasses the particles undergoing the first plastic events are somewhat correlated and approach maximal around the yield, manifesting into the shear band. The individual initial STZ event(s) and their spatial-arrangment indicate their sensitivity upon the preparation history and the local structural properties [40,44,45]. Notably, steady-states depict the universal STZ dynamics, independent of the initial and transient elastoplastic behavior. The overall correlation between the plastic events and cooling effect needs further attention, which we wish to address in the subsequent work with larger samples and cooling rates.

C. Stress drops

As discussed in the introduction, the crackling noise in the stress-strain curve is defined with the drops of stress $\Delta\tau$ and the intervals between those drops $\Delta\gamma$, giving rise to the gap distribution $p(\Delta\gamma)$.

Looking at the stress drops $\Delta\tau$ in different strain windows shows [see Fig. 7(a)] that they follow a power-law distribution with a Gaussian cutoff

$$p(\Delta\tau) \propto \Delta\tau^{-\beta} \exp\left[-\left(\frac{\Delta\tau}{\Delta\tau_0}\right)^2\right], \tag{2}$$

where β is an exponent and $\Delta\tau_0$ the cutoff scale increasing with strain. Figure 7(a) shows the maximum likelihood [41] fits to this distribution where over two decades of power-law scaling with an exponent of 1.16 can be observed for strain intervals after the yield point. This exponent is significantly lower than the mean-field value 3/2 reported in experiments.

Even though the distribution of Eq. (2) fits the data well for all the strain bins, the power-law region is extremely small for small strains. This means that the distributions can be fitted using a light-tailed distribution, as illustrated in the inset of Fig. 7(a) where stress drop distributions for the first three strain bins are plotted using a semilog scale along with an exponential fit. To quantify this we compute the Bayesian information criterion [46,47]

$$\mathrm{BIC} = -2\ln\mathcal{L} + n_\mathrm{p}\ln N_{\Delta\tau}, \tag{3}$$

where $\mathcal{L}$ is the likelihood function, $N_{\Delta\tau}$ the number of stress drop datapoints, and n_p the number of parameters in the chosen distribution. The lower the BIC is, the better the model fits the data. We compute the BIC for a power-law distribution with a Gaussian cutoff [Eq. (2) and $n_\mathrm{p} = 2$] and for a half-Gaussian distribution [where $n_\mathrm{p} = 1$ and $p(\Delta\tau) \propto e^{-(\Delta\tau/\Delta\tau_0)^2}$]. From Fig. 7(b) one can see that both distributions perform roughly equally before the yield point, signifying a lack of a power-law scaling region below this point. After the yield point, the power-law fits the data significantly better.

In the steady state regime (here $\gamma > 0.50$) the stress drop distributions show completely universal behavior (see Fig. 8) for all the cooling rates and compositions. The distribution follows Eq. (2) with the same exponent $\beta = 1.16$ and a universal cutoff value of $\Delta\tau_0 = 0.34$ GPa.

The behavior of the cutoff scale $\Delta\tau_0$ [see Fig. 7(c)] resembles the behavior seen in Fig. 4. When approaching yielding from below, the cutoff scale increases rapidly, reaching a maximum around yielding. The value then slightly decreases to a steady-state value, which is achieved already at around 15% strain.

The behavior of the stress drop cutoff with the system size [Fig. 7(c)] shows a power-law-like scaling below the yield point, roughly system-size independent behavior at yielding, and power-law-like scaling again after yielding.

Looking at the scaling of the average stress drop with the system size [see Fig. 9(a)], one can see fairly robust power-law scaling $\langle\Delta\tau\rangle \propto N^{-\alpha}$. However, the exponent α changes with strain. Two distinct power-law regimes can be recognized [see Fig. 9(b)]. At low strains, below the yield point, the average

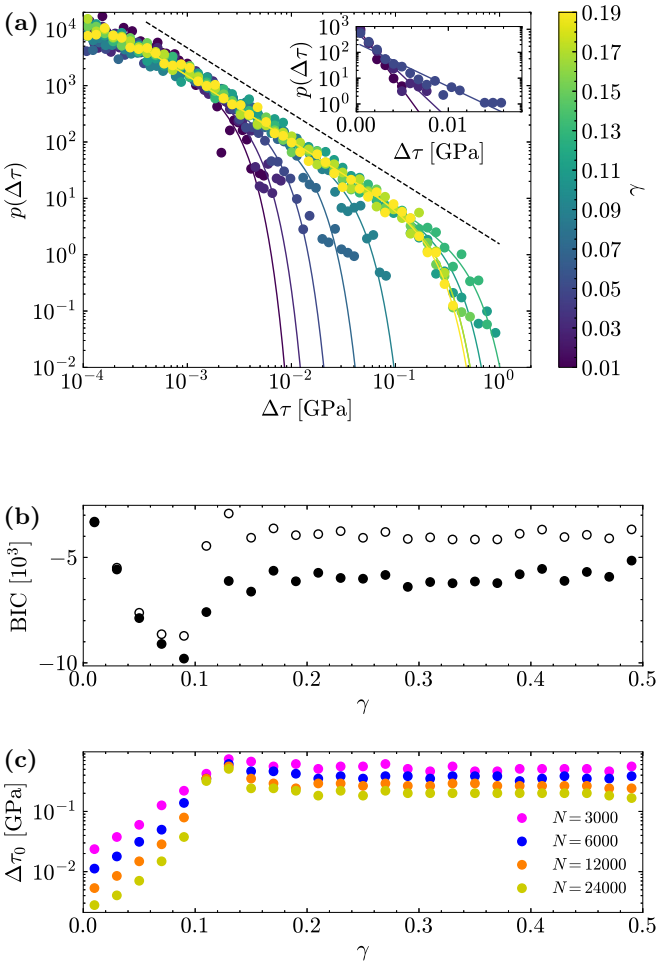

FIG. 7. (a) The stress drop distribution (for the $Cu_{0.50}Zr_{0.50}$, $\dot{T} = 10^{12}$ K/s, $N = 24\,000$ system) for various strain bins indicated by the plot color. The lines are fit to Eq. (2) and the dashed black line shows the pure power-law behavior $p(\Delta\tau) \propto \Delta\tau^{-1.16}$. The inset shows an exponential fit for the three first strain bins, showing the lack of power-law scaling. (b) The BIC [Eq. (3)] as a function of strain for the power law with Gaussian cutoff (solid dots) and the half-Gaussian distribution (hollow dots). (c) The cutoff scale of Eq. (2) as a function of strain for different system sizes.

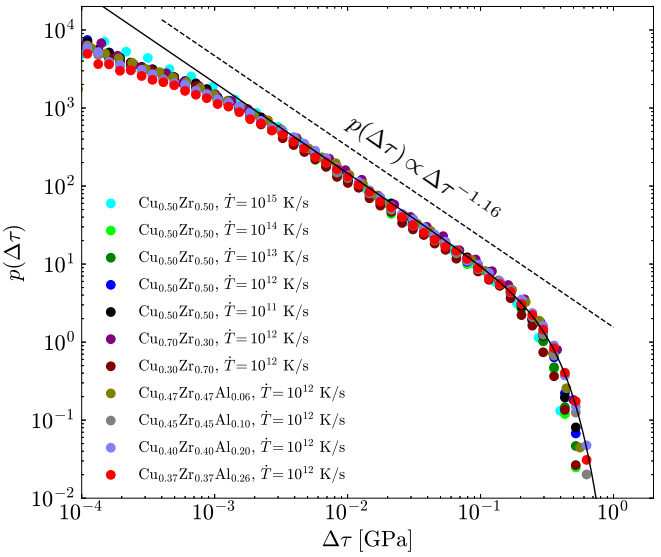

FIG. 8. The steady-state stress drop distribution for different compositions and cooling rates $\dot{T}$ (for $N = 6000$). The solid black line corresponds to a fit to Eq. (2) which gives a universal result with cutoff $\Delta\tau_0 = 0.34$ GPa. The dashed line gives a reference power-law with the exponent $\beta = 1.16$.

stress drop size scales with an exponent $\alpha_1 = 0.81 \pm 0.02$. At high strains, above the yield point and close to the steady state, the exponent value of $\alpha_2 = 0.44 \pm 0.03$ can be found. Around the yield point, the scaling vanishes as the exponent α goes close to zero. For the distribution of Eq. (2) the average value scales approximately as $\langle\Delta\tau\rangle \propto \Delta\tau_0^{1-\beta}$ which is clearly seen in the similar behavior of Figs. 7(c) and 9. When one accounts for the difference in definitions of the average avalanche size (multiplication by a factor N), these exponent values roughly match the results obtained in previous studies [5–7,20].

D. Gap distribution

To characterize the behavior of the pseudogap, we have fitted the gap distribution using the Weibull distribution [see Fig. 10(a)]

$$p(\Delta\gamma) \propto \Delta\gamma^{\theta} \exp\left[-\left(\frac{\Delta\gamma}{\Delta\gamma_0}\right)^{1+\theta}\right], \tag{4}$$

where θ corresponds to the gap exponent and $\Delta\gamma_0$ to the cutoff scale.

The values of the gap exponent start (at low strains) close to $\theta = 0.7$ and rapidly decrease to values around $\theta = 0.3 \pm 0.1$ [see Fig. 10(b)]. The cutoff scale $\Delta\gamma_0$ also starts from a high value, decreases to a minimum value around yielding, and then increases to a steady-state value ([ee Fig. 10(c], mirroring the behavior of the stress drop cutoff $\Delta\tau_0$.

It is noteworthy that the tail of the distribution in the first strain bin does not follow the Weibull distribution very well. Instead, it shows a much wider tail, extending to half of a decade higher values than the distributions of the other strain

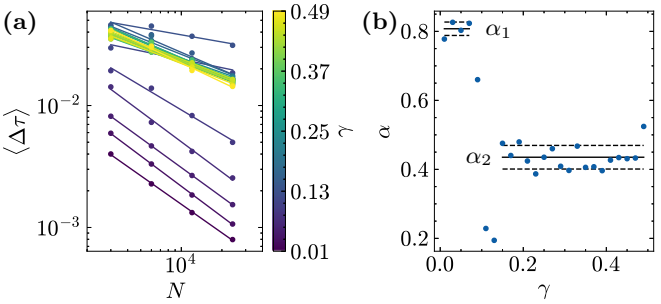

FIG. 9. (a) The average stress drop as a function of the system size for different strain bins is illustrated by the plot color. The lines correspond to power-law fits $\langle\Delta\tau\rangle \propto N^{-\alpha}$. (b) The evolution of the exponent α with the strain. The black lines illustrate the exponent (solid line) and the standard deviation (dashed lines) for the preyield ($\alpha_1 = 0.81 \pm 0.02$) and steady-state regimes ($\alpha_2 = 0.44 \pm 0.03$).

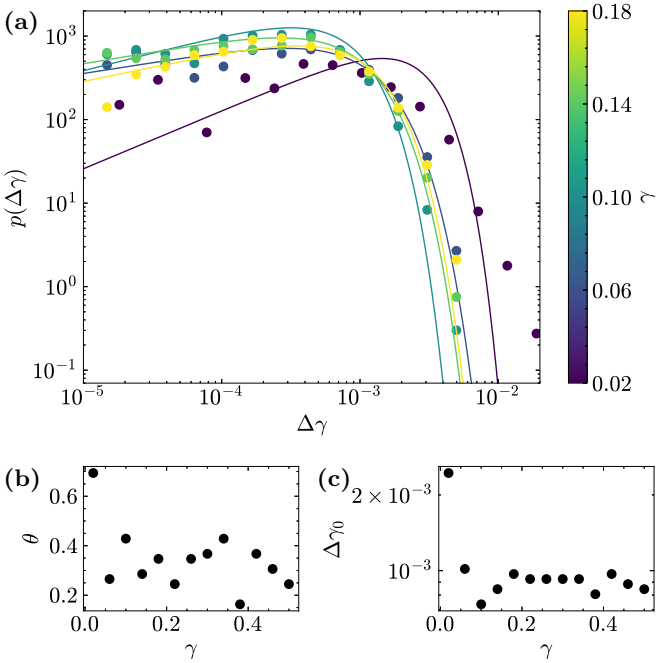

FIG. 10. (a) The gap distribution or the strain interval distribution (for $Cu_{0.50}Zr_{0.50}$, $\dot{T} = 10^{11}$ K/s, $N = 24\,000$) for various strain bins indicated by the plot color. The lines are fitted to Eq. (4). (b) The exponent of Eq. (4) as a function of the strain. (c) The cutoff scale of Eq. (4) as a function of the strain.

bins. This is likely due to the glass preparation, as glasses cooled to 300 K are not fully relaxed. This might cause deviations from the normal behavior, i.e., excess waiting times for initial events. The effect of these excess extreme events is enchanced by the low number of events in the first strain bin.

Figure 11 finally shows in the post-yield regime how the drop rate and "stress production rate" (binned sum of stress drops) scales with $\Delta\gamma$. For very small strain increments, the rates are low and constant in agreement with the trivial assumption of what follows from the gap distribution in this limit. Beyond a strain of about 10^{-3}, both rates start to increase apparently linearly to approach the average event and stress drop rates.

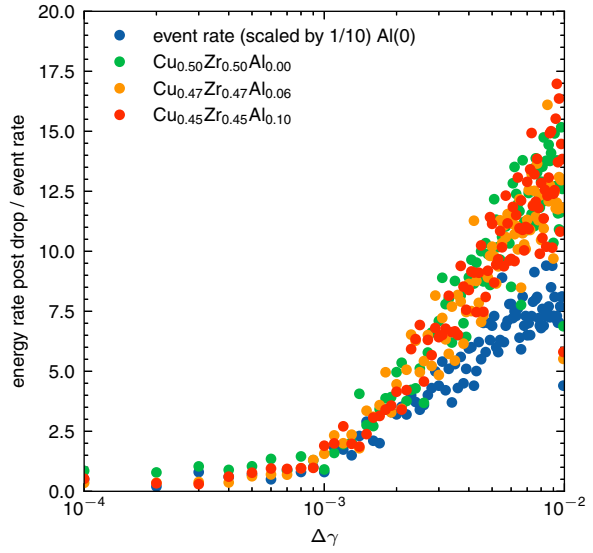

FIG. 11. Post-stress drop correlations in the steady-state flow: event rate, and the stress drop rate for systems with different Al contents.

IV. CONCLUSIONS

Modeling studies of metallic glasses offer a unique advantage in bridging micro- to macroscopic understanding of their mechanical properties. However, these studies have rarely aligned closely with general observations, theoretical frameworks, or direct comparisons with experimental results. Here we have taken a look at the widely studied Cu-Zr-Al system under athermal quasistatic shear, mimicking experimental conditions, regarding the elasticity and avalanches in preyield, at yield transition and in the steady-state flow beyond the yield point. The study is classified into two parts: (i) the effect of cooling and (ii) the role of composition (Cu-Zr-Al) in the mechanical response.

The evolution of plastic deformation exhibits distinct variations depending on the "ageing" of the glass. Notably, both shear modulus and yield strain increase systematically as cooling rates decrease. The initial plastic event, along with the spatial correlations of subvolumes, captures the unique features of system preparation, likely influenced by complex elastic interactions. Across the range of aluminium concentrations, the composition appears to have minimal influence on species contributing to plasticity, as highlighted by stress drops and the behavior of subsystems under deformation. The early time response is typical of virgin disordered systems with a positive gap exponent. However, statistics of stress drops in the steady-state flow are found to be entertainingly superuniversal, with minor discrepancies in the power-law exponents from previous studies [28,29], which need further attention and would be interesting to test in experiments.

ACKNOWLEDGMENTS

T.M. and M.J.A. acknowledge support from FinnCERES flagship (Grant No. 151830423), Business Finland (Grants No. 211835, No. 211909, and No. 211989), and Future Makers programs. M.J.A. acknowledges support from the Academy of Finland Center of Excellence program (Programs No. 278367 and No. 317464), as well as the Finnish Cultural Foundation. A.D.S.P, S.B., and M.J.A. acknowledge support from the European Union Horizon 2020 research and innovation program under Grant Agreement No. 857470 and the European Regional Development Fund via the Foundation for Polish Science International Research Agenda PLUS program under Grant No. MAB PLUS/2018/8. S.B. acknowledges support through SONATABIS Grant No. DEC-2023/50/E/ST3/00569 from the National Science Center in Poland. The authors acknowledge the computational resources provided by the Aalto University School of Science "Science-IT" project.

[1] A. Argon, Plastic deformation in metallic glasses, Acta Metall. **27**, 47 (1979).

[2] M. L. Falk and J. S. Langer, Dynamics of viscoplastic deformation in amorphous solids, Phys. Rev. E **57**, 7192 (1998).

[3] A. Tanguy, F. Leonforte, and J. L. Barrat, Plastic response of a 2D Lennard-Jones amorphous solid: Detailed analysis of the local rearrangements at very slow strain rate, Eur. Phys. J. E **20**, 355 (2006).

[4] B. L. Li, E. R. Homer, and C. A. Schuh, Shear transformation zone dynamics model for metallic glasses incorporating free volume as a state variable, Acta Mater. **61**, 3347 (2013).

[5] A. Lemaître and C. Caroli, Plastic response of a 2D amorphous solid to quasi-static shear : II - Dynamical noise and avalanches in a mean field model, arXiv:0705.3122.

[6] S. Karmakar, E. Lerner, and I. Procaccia, Statistical physics of the yielding transition in amorphous solids, Phys. Rev. E **82**, 055103(R) (2010).

[7] H. G. E. Hentschel, P. K. Jaiswal, I. Procaccia, and S. Sastry, Stochastic approach to plasticity and yield in amorphous solids, Phys. Rev. E **92**, 062302 (2015).

[8] J. Lin, E. Lerner, A. Rosso, and M. Wyart, Scaling description of the yielding transition in soft amorphous solids at zero temperature, Proc. Natl. Acad. Sci. USA **111**, 14382 (2014).

[9] J. Lin, T. Gueudré, A. Rosso, and M. Wyart, Criticality in the approach to failure in amorphous solids, Phys. Rev. Lett. **115**, 168001 (2015).

[10] J. Lin and M. Wyart, Mean-field description of plastic flow in amorphous solids, Phys. Rev. X **6**, 011005 (2016).

[11] J.-C. Baret, D. Vandembroucq, and S. Roux, Extremal model for amorphous media plasticity, Phys. Rev. Lett. **89**, 195506 (2002).

[12] A. Nicolas, E. E. Ferrero, K. Martens, and J.-L. Barrat, Deformation and flow of amorphous solids: Insights from elastoplastic models, Rev. Mod. Phys. **90**, 045006 (2018).

[13] A. Rosso, J. P. Sethna, and M. Wyart, Avalanches and deformation in glasses and disordered systems, arXiv:2208.04090.

[14] K. M. Salerno and M. O. Robbins, Effect of inertia on sheared disordered solids: Critical scaling of avalanches in two and three dimensions, Phys. Rev. E **88**, 062206 (2013).

[15] M. Ozawa, L. Berthier, G. Biroli, A. Rosso, and G. Tarjus, Random critical point separates brittle and ductile yielding transitions in amorphous materials, Proc. Natl. Acad. Sci. USA **115**, 6656 (2018).

[16] B. A. Sun, H. B. Yu, W. Jiao, H. Y. Bai, D. Q. Zhao, and W. H. Wang, Plasticity of ductile metallic glasses: A self-organized critical state, Phys. Rev. Lett. **105**, 035501 (2010).

[17] T. Niiyama, M. Wakeda, T. Shimokawa, and S. Ogata, Structural relaxation affecting shear-transformation avalanches in metallic glasses, Phys. Rev. E **100**, 043002 (2019).

[18] S. Cui, H. Liu, and H. Peng, Anisotropic correlations of plasticity on the yielding of metallic glasses, Phys. Rev. E **106**, 014607 (2022).

[19] A. Lagogianni, C. Liu, K. Martens, and K. Samwer, Plastic avalanches in the so-called elastic regime of metallic glasses, Eur. Phys. J. B **91**, 104 (2018).

[20] B. Shang, P. Guan, and J.-L. Barrat, Elastic avalanches reveal marginal behavior in amorphous solids, Proc. Natl. Acad. Sci. USA **117**, 86 (2020).

[21] A. Inoue and W. Zhang, Formation, thermal stability and mechanical properties of Cu-Zr-Al bulk glassy alloys, Mater. Trans. **43**, 2921 (2002).

[22] J. Das, M. B. Tang, K. B. Kim, R. Theissmann, F. Baier, W. H. Wang, and J. Eckert, "Work-hardenable" ductile bulk metallic glass, Phys. Rev. Lett. **94**, 205501 (2005).

[23] P. Yu and H. Bai, Poisson's ratio and plasticity in CuZrAl bulk metallic glasses, Mater. Sci. Eng.: A **485**, 1 (2008).

[24] S. Pauly, S. Gorantla, G. Wang, U. Kühn, and J. Eckert, Transformation-mediated ductility in CuZr-based bulk metallic glasses, Nat. Mater. **9**, 473 (2010).

[25] C. Poltronieri, A. Brognara, F. Bignoli, S. Evertz, P. Djemia, D. Faurie, F. Challali, C. Li, L. Belliard, G. Dehm, J. Best, and M. Ghidelli, Mechanical properties and thermal stability of $ZrCuAl_x$ thin film metallic glasses: Experiments and first-principle calculations, Acta Mater. **258**, 119226 (2023).

[26] T. Cheung and C. Shek, Thermal and mechanical properties of Cu–Zr–Al bulk metallic glasses, J. Alloys Compd. **434-435**, 71 (2007).

[27] H. Sun, Z. Ning, J. Ren, W. Liang, Y. Huang, J. Sun, X. Xue, and G. Wang, Serration and shear avalanches in a ZrCu based bulk metallic glass composite in different loading methods, J. Mater. Sci. Technol. **35**, 2079 (2019).

[28] K. Tao, F. Li, Y. Liu, E. Pineda, K. Song, and J. Qiao, Distinct avalanche dynamics detected in metallic glasses with high energy state revealing the crack-like shear banding mechanism, Int. J. Plast. **174**, 103873 (2024).

[29] J. P. Coleman, F. Meng, K. Tsuchiya, J. Beadsworth, M. LeBlanc, P. K. Liaw, J. T. Uhl, R. L. Weaver, and K. A. Dahmen, Effect of annealing on nanoindentation slips in a bulk metallic glass, Phys. Rev. B **96**, 134117 (2017).

[30] J. Antonaglia, W. J. Wright, X. Gu, R. R. Byer, T. C. Hufnagel, M. LeBlanc, J. T. Uhl, and K. A. Dahmen, Bulk metallic glasses deform via slip avalanches, Phys. Rev. Lett. **112**, 155501 (2014).

[31] W. J. Wright, Y. Liu, X. Gu, K. D. Van Ness, S. L. Robare, X. Liu, J. Antonaglia, M. LeBlanc, J. T. Uhl, T. C. Hufnagel *et al.*, Experimental evidence for both progressive and simultaneous shear during quasistatic compression of a bulk metallic glass, J. Appl. Phys. **119**, 084908 (2016).

[32] D. V. Denisov, K. A. Lőrincz, W. J. Wright, T. C. Hufnagel, A. Nawano, X. Gu, J. T. Uhl, K. A. Dahmen, and P. Schall, Universal slip dynamics in metallic glasses and granular matter–linking frictional weakening with inertial effects, Sci. Rep. **7**, 43376 (2017).

[33] A. A. Long, D. V. Denisov, P. Schall, T. C. Hufnagel, X. Gu, W. J. Wright, and K. A. Dahmen, From critical behavior to catastrophic runaways: Comparing sheared granular materials with bulk metallic glasses, Granular Matter **21**, 99 (2019).

[34] J. Antonaglia, X. Xie, G. Schwarz, M. Wraith, J. Qiao, Y. Zhang, P. K. Liaw, J. T. Uhl, and K. A. Dahmen, Tuned critical avalanche scaling in bulk metallic glasses, Sci. Rep. **4**, 4382 (2014).

[35] Y. Luo, J. Li, Z. Wang, M. Zhang, and J. Qiao, Strain rate-dependent avalanches in bulk metallic glasses, J. Alloys Compd. **864**, 158107 (2021).

[36] A. P. Thompson, H. M. Aktulga, R. Berger, D. S. Bolintineanu, W. M. Brown, P. S. Crozier, P. J. in 't Veld, A. Kohlmeyer, S. G. Moore, T. D. Nguyen, R. Shan, M. J. Stevens, J. Tranchida, C. Trott, and S. J. Plimpton, LAMMPS - A flexible simulation tool for particle-based materials modeling at the atomic, meso, and continuum scales, Comp. Phys. Comm. **271**, 108171 (2022).

[37] Y. Q. Cheng, E. Ma, and H. W. Sheng, Atomic level structure in multicomponent bulk metallic glass, Phys. Rev. Lett. **102**, 245501 (2009).

[38] B. Sadigh, P. Erhart, A. Stukowski, A. Caro, E. Martinez, and L. Zepeda-Ruiz, Scalable parallel Monte Carlo algorithm for atomistic simulations of precipitation in alloys, Phys. Rev. B **85**, 184203 (2012).

[39] R. Alvarez-Donado, S. Bonfanti, and M. Alava, Simulated multi-component metallic glasses akin to experiments, arXiv:2309.05806.

[40] Z. Zhang, J. Ding, and E. Ma, Shear transformations in metallic glasses without excessive and predefinable defects, Proc. Natl. Acad. Sci. USA **119**, e2213941119 (2022).

[41] J. Baró and E. Vives, Analysis of power-law exponents by maximum-likelihood maps, Phys. Rev. E **85**, 066121 (2012).

[42] T. B. Schrøder, S. Sastry, J. C. Dyre, and S. C. Glotzer, Crossover to potential energy landscape dominated dynamics in a model glass-forming liquid, J. Chem. Phys. **112**, 9834 (2000).

[43] P. Leishangthem, A. D. Parmar, and S. Sastry, The yielding transition in amorphous solids under oscillatory shear deformation, Nat. Commun. **8**, 14653 (2017).

[44] A. R. Hinkle, C. H. Rycroft, M. D. Shields, and M. L. Falk, Coarse graining atomistic simulations of plastically deforming amorphous solids, Phys. Rev. E **95**, 053001 (2017).

[45] D. Richard, M. Ozawa, S. Patinet, E. Stanifer, B. Shang, S. A. Ridout, B. Xu, G. Zhang, P. K. Morse, J. L. Barrat, L. Berthier, M. L. Falk, P. Guan, A. J. Liu, K. Martens, S. Sastry, D. Vandembroucq, E. Lerner, and M. L. Manning, Predicting plasticity in disordered solids from structural indicators, Phys. Rev. Mater. **4**, 113609 (2020).

[46] T. Leonard and J. S. Hsu, *Bayesian Methods: An Analysis for Statisticians and Interdisciplinary Researchers* (Cambridge University Press, Cambridge, UK, 2001), Vol. 5.

[47] T. Mäkinen, J. Weiss, D. Amitrano, and P. Roux, History effects in the creep of a disordered brittle material, Phys. Rev. Mater. **7**, 033602 (2023).